Pergamon

Acta mater. 49 (2001) 4325–4335

Acta MATERIALIA

www.elsevier.com/locate/actamat

THE COMPACTION OF A RANDOM DISTRIBUTION OF METAL CYLINDERS BY THE DISCRETE ELEMENT METHOD

Pia REDANZ[1]† and Norman A. FLECK[2]

[1]Department of Mechanical Engineering, Solid Mechanics, Technical University of Denmark, 2800 Lyngby, Denmark and [2]Cambridge University Engineering Department, Trumpington Street, Cambridge CB2 1PZ, UK

(Received 23 May 2001; received in revised form 24 July 2001; accepted 24 July 2001)

Abstract—The cold compaction of a 2D random distribution of metal circular cylinders has been investigated numerically by the discrete element method. Each cylindrical particle is located by a node at its centre and the plastic indentation of the contacts between neighbouring particles is represented by non-linear springs. The initial packing of the particles is generated by the ballistic deposition method. Salient micromechanical features of closed die and isostatic powder compaction are elucidated for both frictionless and sticking contacts. It is found that substantial rearrangement of frictionless particles takes place, leading to yield surfaces of similar shape but about half the size of that found for affine motion, as reported in [*J. Mech. Phys. Solids* 40 (1992) 1139; 43 (1995) 1409; 47 (1999) 785]. An increase in the level of inter-particle friction leads to a reduction in the degree of local particle rearrangement: the relative displacement of particle centres in the network is more closely represented by affine motion for the case of sticking contacts than frictionless contacts. The discrete element calculations suggest that the yield surfaces for sticking contacts are similar in shape to those for frictionless particles, but are about double the size.

Keywords: Powder consolidation; Metals

1. INTRODUCTION

The cold compaction and subsequent sintering of metal powder is a widely used production method for small, complex parts in the automotive industry. This process route makes it possible to produce near net shape components of complex geometry and high strength. Recently, the compaction and sintering of parts of simple shape have been simulated using the finite element method with various macroscopic constitutive descriptions of material response, see for example [4–7].

In the present study, we shall focus on the initial phase of powder compaction, termed stage I, wherein isolated plastic contacts between particles control the macroscopic deformation. Subsequently, plasticity spreads throughout the particles from contact to contact, and the contacts no longer deform in an isolated manner. In the final phase of compaction porosity exists in the form of isolated voids; this is known as stage II. Ashby and co-workers [8–10] have used indentation theory at each particle contact in order to predict the pressure versus relative density curve for hydrostatic stage I compaction. They assumed that the porous aggregate consists of randomly packed, rigid-perfectly plastic spheres of equal diameter and joined by discrete necks. Fleck *et al*. [1] generalised this approach to multi-axial stress states and Fleck [2] included the effects of deformation-induced anisotropy and inter-particle cohesion. Recently, Storåkers *et al.* [3] have extended this model to powder composites which deform in a power law visco-plastic manner.

The material models described above are based upon micromechanical assumptions such as the affine deformation of particles prescribed by the macroscopic strain with no local rearrangement of particles. In the present work, a model has been used to investigate the validity of these assumptions for a random distribution of circular cylindrical particles of given size distribution; yield surfaces for both isostatic and closed die compaction are determined, and are compared with the upper bound yield surfaces for cylindrical particles based upon affine motion [1–3]. A similar discrete element model has been used in [11] for sintering. In general metal powders have very low inter-particle tensile strength thus we will limit our studies to powders with zero inter-particle cohesive strength.

† To whom all correspondence should be addressed.
E-mail address: pia@mek.dtu.dk (P. Redanz)

1359-6454/01/$20.00
PII: S1359-6454(01)00298-1

The discrete element method allows us to explore the significance of non-affine particle motion, by the local rolling and sliding at contacts, upon the macroscopic compaction response. For example, previous estimates [1–3] based upon affine motion suggest that a vertex forms at the loading point of the yield surface. It is of both fundamental and practical significance to determine the sensitivity of the macroscopic response to the degree of local particle rearrangement.

2. NUMERICAL METHOD

2.1. Particle–particle formulation

Consider an array of circular cylinders of unit depth. Two representative cylinders 1 and 2 are in contact, and have radii R_1 and R_2, as shown in Fig. 1(a). The contact force between the two cylinders is resolved into a normal force F_N acting along the common normal to the plane of contact, and a tangential force F_T due to friction. The rolling moment M is neglected since the area of contact is small for stage I compaction.

Each contact is represented by a generalised spring element, with each particle centre represented by a node as shown in Fig. 1(b); the constitutive law for the spring is detailed below. The tangential force F_T at each contact generates a moment $M_i = -d_i F_T$ at the centre of the contacting particle, where d_i is the distance from the centre of particle i to the contact.

2.1.1. Normal direction. The incremental approach of one particle with respect to its neighbour is expressed by

$$\dot{u}_N = \dot{u}_{N1} - \dot{u}_{N2} \tag{1}$$

where $\dot{u}_{N1}$ and $\dot{u}_{N2}$ are the incremental displacements of particles 1 and 2, respectively, along the contact normal as defined in Fig. 2.

Particle deformation during compaction occurs by the plastic flattening of contacts. We assume that the normal pressure p at each contact in a rigid-perfectly plastic material under plane strain conditions equals the Prandtl value of three times the yield strength σ_y of the solid, $p = 3\sigma_y$. Hence, the normal force versus particle overlap relationship has the form

$$F_N = 3\sigma_y A_c \text{ with } A_c = \sqrt{8 u_N R_1 R_2/(R_1 + R_2)} \tag{2}$$

where A_c is the contact area per unit depth of two cylinders overlapping by u_N. Since the force–displacement law (2) is nonlinear, an incremental form is employed,

$$\dot{F}_N = 3\sigma_y \sqrt{\frac{R_1 + R_2}{2u_N}}\dot{u}_N \tag{3}$$

with the incremental normal force on each node written as

$$\dot{F}_{N1} = -\dot{F}_{N2} = \dot{F}_N \tag{4}$$

according to the sign convention of Fig. 2. A similar kinematic formulation in the normal direction has

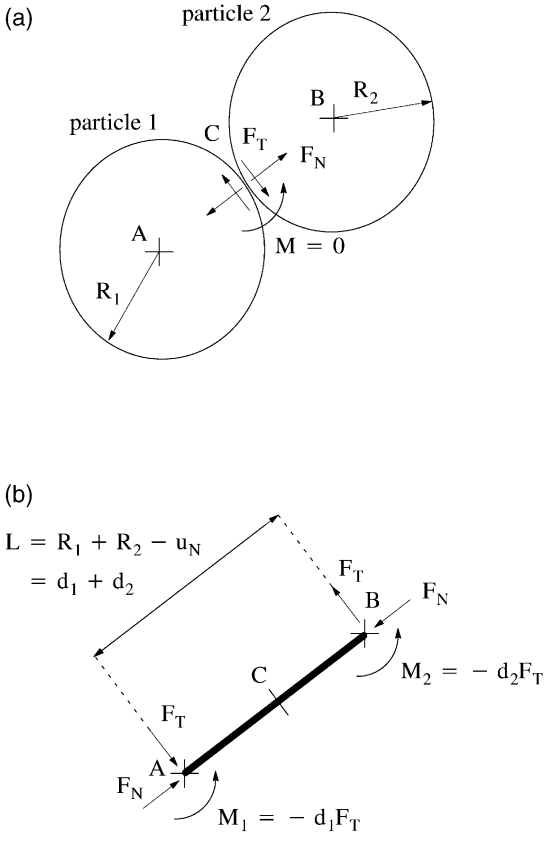

Fig. 1. Two-particle model. (a) Two cylinders of radii R_1 and R_2 in contact. The contact forces in the normal and tangential directions are denoted F_N and F_T respectively. The rolling moment, M, at the contact is set to zero since the area of contact remains small. (b) The spring element reresenting the contact. Here u_N is the relative displacement in the direction normal to the plane of contact.

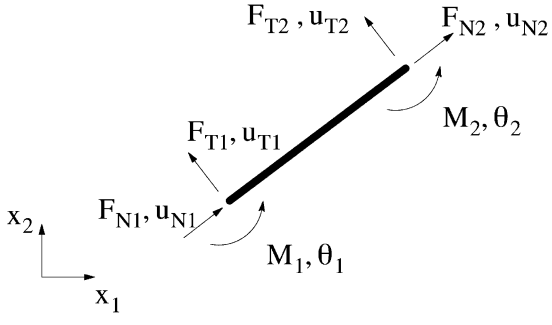

Fig. 2. Spring element defining directions of nodal displacements, forces, rotations and moments.

been used previously in [12–14] for the compaction of spheres.

2.1.2. Tangential direction. The sliding component of the displacement increment of one particle with respect to its contacting neighbour (i.e. the slip rate) is given by

$$\dot{u}_T = \dot{u}_{T1} - \dot{u}_{T2} + d_1\dot{\theta}_1 + d_2\dot{\theta}_2 \tag{5}$$

where $\dot{u}_{T1}$ and $\dot{u}_{T2}$ are the tangential displacement increments of the centres of particles 1 and 2, respectively, and the additional contribution to the sliding rate comes from the particle spins $\dot{\theta}_i$.

A friction law is enforced via tangential elastic springs of stiffness, k_T, such that the shear stress at the contact is related to the relative sliding displacement u_T by

$$\tau \equiv F_T/A_c = k_T u_T \text{ for } |F_T| < \mu |F_N| \tag{6}$$

where μ is the Coulomb friction coefficient. The spring constant k_T is taken to be sufficiently large that each contact is either in a sticking state, with negligible relative displacement, or in a state of gross slip with

$$F_T = -sgn(\dot{u}_T)\mu F_N \tag{7}$$

Tangential stresses exceeding the shear yield stress, τ_y, of the matrix material are unrealistic, and so an upper limit of the shear stress, $\tau_{max} = \tau_y = \sigma_y/\sqrt{3}$, is imposed.

Equilibrium dictates that the tangential nodal forces are

$$-\dot{F}_{T1} = \dot{F}_{T2} = \dot{F}_T \tag{8}$$

with each node experiencing a moment due to the tangential force, $\dot{F}_T$, at the particle periphery such that

$$\dot{M}_1 = -d_1\dot{F}_T \text{ and } \dot{M}_2 = -d_2\dot{F}_T \tag{9}$$

2.2. Generation of the random packing

The initial packings of the particles have been generated by a ballistic deposition method, as detailed for example in the Appendix of [15]. We believe that this method provides realistic initial packings for powders laid down in a die before compaction. The particles are dropped one by one from a random starting position into a container, and each particle follows the path of steepest descent. The packing simulation is purely geometric and inertial forces are neglected in predicting the motion of the particles. When a particle has attained static equilibrium, its position is fixed and a new particle is dropped until the box has filled with particles.

A typical packing of monosized particles of radius $r = R$ is shown in Fig. 3(a), with the width W of the square box taken as $W = 80R$. The packing consists of 1683 particles (nodes) and 3279 contacts (elements) and has an initial relative density $D_0 = 0.823$; the relative density of the aggregate is defined by the ratio of the total cross-sectional area of the cylinders to that of the box. Each inter-particle contact is represented by a line between neighbouring particle centres in the insert of Fig. 3(a). It is seen that the monosized cylinders pack in a crystalline manner, as noted previously by [16, 17] for example. In contrast, a more random packing occurs when the particle radii are dispersed slightly: Fig. 3(b) shows a typical packing for the case where the radius of each particle varies randomly from $r = 0.9R$ to $1.1R$. The aggregate comprises 1644 particles and 3183 elements, and has a relative density $D_0 = 0.814$ which is slightly less than that for the crystalline packing of Fig. 3(a). Numerical experimentation suggested that a box width of $W = 80R$ is sufficiently large for the relative density to be independent of W for the dispersed particle packing.

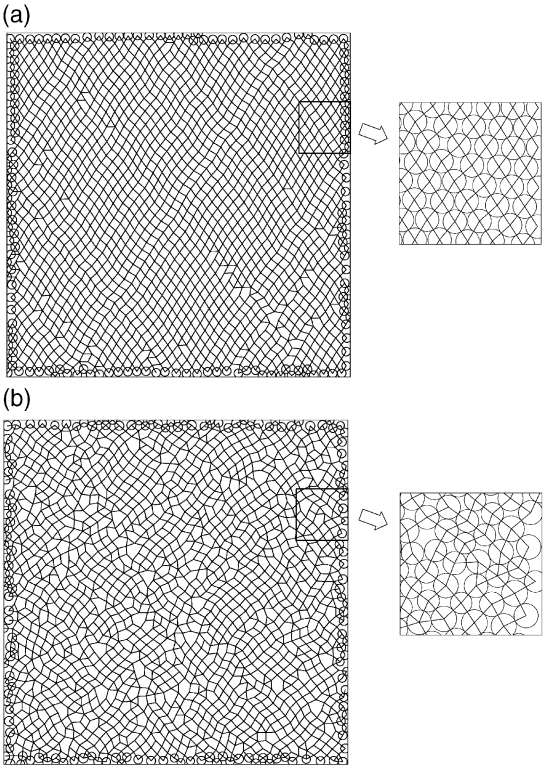

Fig. 3. Initial packings of cylinders. Each line represents a contact and each junction represents a cylinder center. (a) Monosized cylinders of radius, $r = R$, where $R/W_{box} = 1.25\times10^{-2}$; 1683 nodes, 3279 elements and the initial density, $D_0 = 0.823$. (b) Cylinders of radius, $r = R[0.9,1.1]$; 1644 nodes, 3183 elements and the initial density $D_0 = 0.814$.

2.3. The discrete element model

We denote the vector (F_N,F_T,M) of generalised force of particle q upon particle p by the symbol f_i^{pq}. Then, equilibrium of forces and moments on the central node of particle p is expressed by

$$\sum_{q=1}^{N_p} f_i^{pq} = 0 \;\forall\; p = 1,N_{tot} \tag{10}$$

where N_p is the number of contacts for each particle p, and the total number of particles is N_{tot}. During compaction, new contacts between the particles are formed and so N_p increments.

The nonlinear form of the interparticle generalised force–displacement relations [equations (2) (6) and (7)] dictates an incremental numerical solution of the equilibrium equation (10). Furthermore, the finite rotation of the contacts and the creation of new contacts during compaction necessitate an incremental numerical scheme such as forward Euler integration. Equations (1–10) lead to the following set of equations for each contact,

$$k_{ij}\begin{Bmatrix}\dot{u}_{N1}\\ \dot{u}_{T1}\\ \dot{\theta}_1\\ \dot{u}_{N2}\\ \dot{u}_{T2}\\ \dot{\theta}_2\end{Bmatrix} = \begin{Bmatrix}\dot{F}_{N1}\\ \dot{F}_{T1}\\ \dot{M}_1\\ \dot{F}_{N2}\\ \dot{F}_{T2}\\ \dot{M}_2\end{Bmatrix} \tag{11}$$

where k_{ij} is the incremental stiffness matrix for a given contact. A global stiffness matrix, A_{ij}, is assembled for the network, such that

$$A_{ij}\dot{D}_i = \dot{F}_i^{applied} \tag{12}$$

where $\dot{D}_i$ are the generalised displacement increments, and $(F_N,F_T,M)_i$ and $\dot{F}_i^{applied}$ are the work-conjugate generalised forces for each particle i. This set of linear equations is solved for the unknown incremental particle displacements and rotations. After each loading increment, the state of the aggregate and thus the global stiffness matrix is updated; the procedure is repeated until the desired density or geometry has been attained. The macroscopic stresses are calculated via the formula ([18])

$$\Sigma_{ij} = \frac{1}{V}\sum_{p=1}^{N_{tot}} F_i^{applied}x_j \tag{13}$$

where x_i are the global coordinates of the centers of the particles and V is the volume per unit depth of the box.

2.4. Boundary conditions

The displacement boundary conditions have the following form

$$\dot{u}_1 = \dot{E}_{11}x_1 + \dot{E}_{12}x_2 \tag{14}$$

$$\dot{u}_2 = \dot{E}_{12}x_1 + \dot{E}_{22}x_2 \tag{15}$$

where $\dot{E}_{ij}$ is the macroscopic strain rate tensor and (x_1,x_2) are the global coordinates of the particle centers. We study both die compaction where equations (14) and (15) are applied to only the layer of peripheral particles, see Fig. 3, and affine compaction where equations (14) and (15) are prescribed to all particles of the network. In both cases, the rotation of particles in the peripheral layer is prevented in order to avoid uncontrolled particle spin. In the following, we shall focus upon "hydrostatic compaction" where the displacement boundary conditions (14) and (15) entail $\dot{E}_{11} = \dot{E}_{22}$, $\dot{E}_{12} = 0$, and uniaxial "closed die compaction" such that $\dot{E}_{22}<0$ and $\dot{E}_{11} = \dot{E}_{12} = 0$.

3. RESULTS AND DISCUSSION

3.1. Macroscopic stresses

The normalised macroscopic stresses, Σ_{ij}/σ_y, for hydrostatic die compaction of the packings shown in Fig. 3 are plotted as a function of relative density D in Fig. 4. The inter-particle contacts are taken to be either frictionless, $\mu = 0$, or sticking, $\mu = \infty$, with the shear stresses at each contact limited by the shear yield strength of the solid. As noted above, the initial density of the monosized cylinders packing is higher than that of the polydispersed packing. For both distributions the ballistic deposition method leads to an

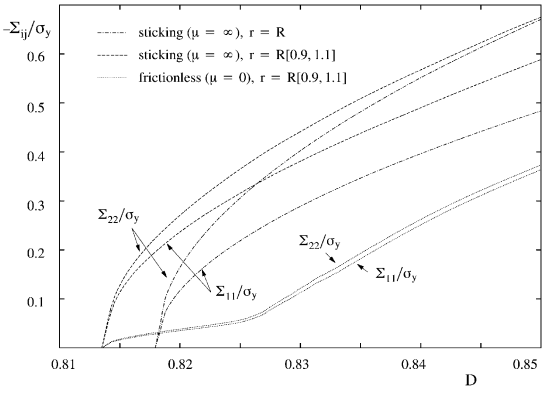

Fig. 4. Normalised macroscopic stresses, Σ_{ij}/σ_y, versus density, D, for hydrostatic compaction of both networks shown in Fig. 3. Results are shown for both monosized particles, $r = R$, and a uniform dispersion in particle radius from $r = 0.9R$ to $r = 1.1R$, labelled $r = R[0.9,1.1]$.

initial packing which is slightly anisotropic, with a more efficient packing in the deposition direction 2 than in the transverse direction 1. Consequently, the stress–density response of the monosized particles undergoing hydrostatic straining is anisotropic: for the monosized packing with sticking contacts Σ_{22} exceeds Σ_{11} by about 40% whereas for the polydispersed packing the stress in the vertical direction, Σ_{22}, is approximately 15% greater than Σ_{11}; this difference is even smaller for the frictionless particles. Repeat simulations confirmed this degree of anisotropy. Since the level of anisotropy is less for the polydispersed packing, we will make use of this particle arrangement from now on.

The effect of friction level upon the hydrostatic and closed die compaction of the polydispersed packing of Fig. 3 are shown in Fig. 5(a) and (b), respectively. Consider first the hydrostatic case in Fig. 5(a): the stress in the vertical direction, Σ_{22} to achieve a given relative density D drops by only 10% when μ is decreased from ∞ to 0.1. (The reason for this is clear: the maximum shear traction for the case of sticking friction equals the shear yield strength $\tau_{max} = \tau_y = \sigma_y/\sqrt{3}$, while the maximum contact pressure equals $3\sigma_y$, giving an effective coefficient of friction of $1/(3\sqrt{3}) = 0.192$. Thus, an assumed friction coefficient of $\mu = \infty$ gives rise to an effective friction coefficient only slightly greater than the value $\mu = 0.1$.) For the case of vanishing interparticle friction, $\mu = 0$, the stress increases only slightly in the beginning of compaction due to substantial rearrangement of the particles, until at $D = 0.825$ the particles have consolidated and the compaction pressure has a sharp up-turn in value. The solid curve in Fig. 5 represents the case of affine deformation (14) and (15) of all particles in the network; under hydrostatic straining, affine deformation gives only normal relative motion between particles, and so the solution is independent of the assumed level of interparticle friction. It is recalled that the imposition of affine deformation leads to an upper bound for the compaction pressure at any given state of particle arrangement. However, non-affine deformation allows for the possibility of rearrangement of particles during compaction, and results in an evolution of compaction pressure which may or may not exceed that for affine deformation. For example, the compaction curve in Fig. 5 for non-affine deformation with sticking contacts ($\mu = \infty$) is comparable to the compaction curve for affine deformation; in contrast, the compaction curve for the frictionless case is at most half that for affine deformation. The effect of constraining the individual particles against rotation has also been explored. For illustration, consider the case of non-affine deformation with sticking contacts; the prevention of particle rotation leads to increased tangential sliding at the contacts and thereby to enhanced plastic dissipation and to a stiffer response by about 10%, see Fig. 5(a).

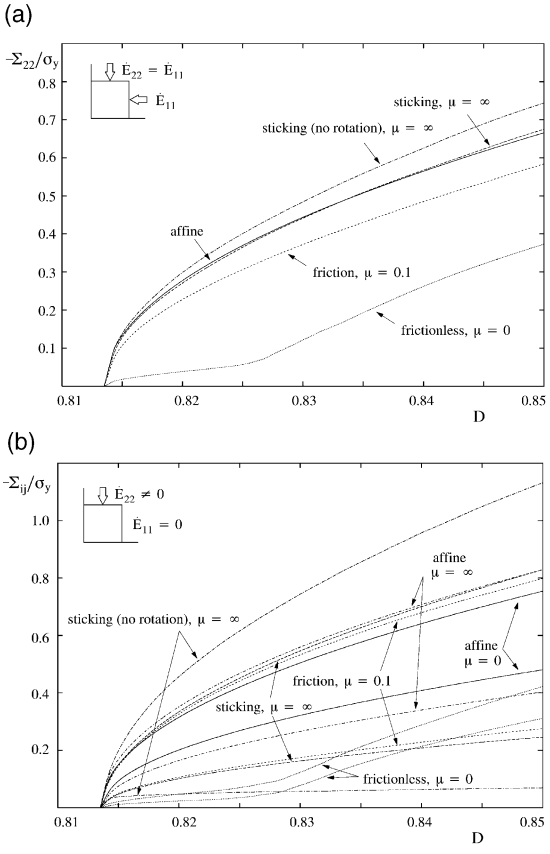

Fig. 5. Normalised macroscopic stresses versus density, D, of the polydispersed packing, $r = R[0.9,1.1]$, Fig. 3(b), for various boundary conditions and degrees of friction. (a) Hydrostatic compaction, Σ_{22}/σ_y, (b) closed die compaction, Σ_{22}/σ_y (upper curves) and Σ_{11}/σ_y (lower curves).

The stress–density response for the polydispersed packing undergoing uniaxial closed die compaction is shown in Fig. 5(b). Consistently, the stress Σ_{22} in the punch direction is higher than that in the transverse direction: this is due to the development of larger contacts with unit normal along the deposition direction 2 than along the transverse direction 1, as noted previously by Fleck [2] and by Storåkers *et al.* [3]. The difference in stress in the two directions is fairly small for frictionless particles, $\mu = 0$, but increases with increasing degree of inter-particle friction. The maximum difference occurs for sticking particles with the additional constraint of no rotation imposed. In contrast to the previous case of hydrostatic compaction, the closed die compaction response for affine deformation (14) and (15) depends upon the degree of friction as non-zero tangential relative motion is now prescribed: the stress difference is smaller for frictionless particles than for sticking contacts.

3.2. Evolution of co-ordination number with degree of hydrostatic and closed die compaction

Consider a polydispersed packing with an initial co-ordination number $Z = 4.0$ by the ballistic deposition method; Z varies with the degree of compaction as shown in Fig. 6(a) for hydrostatic compaction and

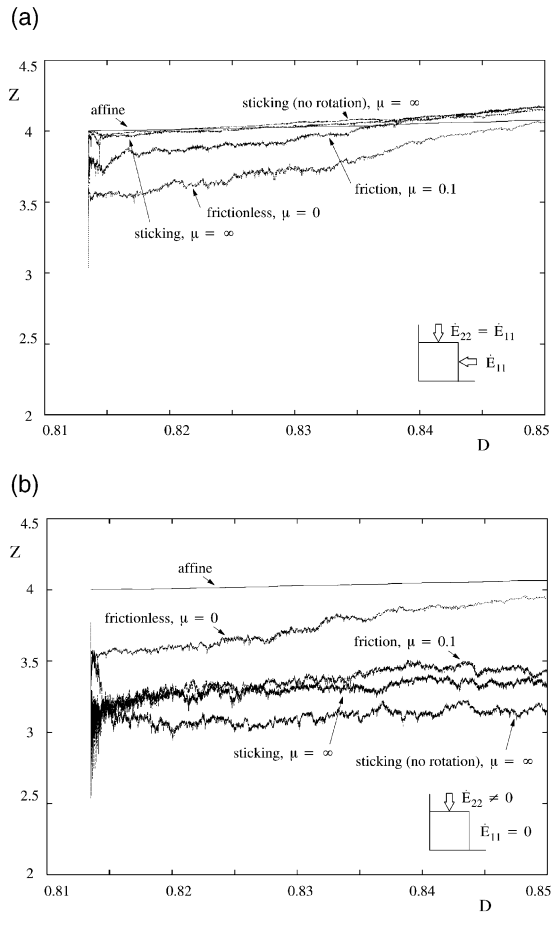

Fig. 6. Average number of contacts per particle (co-ordination number), Z, versus density, D, of the network shown in Fig. 3(b) undergoing compaction. Results of various degrees of inter-particle friction and boundary conditions are shown for (a) hydrostatic compaction and (b) closed die compaction.

in Fig. 6(b) for closed die compaction. Results for selected levels of friction are shown in these figures, and the errors introduced by the affine deformation assumption and by constraint against particle rotation are explored. We shall take the affine deformation case as the reference solution; then, the co-ordination number Z increases slightly from 4.0 to 4.1 as D increases from 0.815 to 0.85, for both hydrostatic and closed die compaction. For the case of hydrostatic compaction, the value of Z is relatively insensitive to imposition of the affine deformation assumption, to constraint against particle rotation and to the assumed friction level: as μ is decreased from the sticking case $\mu = \infty$ to the frictionless case $\mu = 0$, the co-ordination number drops by at most 0.5 during stage I compaction.

In contrast, for closed die compaction, a relaxation of the affine deformation assumption leads to a rapid drop in Z-value from 4 to about 3.0 to 3.5, depending upon the friction level. In the early stages of compaction Z decreases from about 3.5 to about 3.0 as the friction coefficient μ is increased from the frictionless limit ($\mu = 0$) to the sticking case ($\mu = \infty$), with an additional slight drop in Z-value when constraint against particle rotation is imposed. As compaction proceeds, the particles with inter-particle friction do not easily rearrange, and contacts normal to the transverse 1-direction enlarge much more slowly than contacts normal to the pressing direction, 2. Consequently, the stress in the pressing direction, Σ_{22}, increases much more rapidly than the stress in the horizontal direction, Σ_{11}, see Fig. 5(b). In contrast, for the frictionless case, the contacts perpendicular to the pressing direction form easily, resulting in a higher average coordination number and a much smaller stress difference in the two directions as seen in Fig. 5(b).

3.3. The significance of local rearrangement of particles

As noted above, affine motion is a major simplifying assumption in several powder compaction models (for example those of Fleck [2] and Storåkers *et al.* [3]): local particle rearrangement is neglected and the centres of particles undergo an affine displacement u_i^A prescribed directly by the macroscopic strain $u_i^A = E_{ij}x_j$. The relative approach of two contacting cylinders can then be expressed as

$$u_N^A = -E_{ij}n_in_j(R_1 + R_2) \tag{16}$$

where n_i is the common unit normal to the contact. The extent to which the relative motion of particles in the discrete element simulations deviate from affine motion has been investigated as follows. A useful non-dimensional measure of the accuracy of the affine assumption is the ensemble average of the difference between the inter-particle approach in a discrete element calculation, u_N, and the approach under affine motion, u_N^A, each normalised by u_N^A; this is shown as a function of relative density D in Fig. 7(a) (b) for hydrostatic and closed die compaction, respectively, of the polydispersed initial packing of Fig. 3(b). For both frictionless hydrostatic and frictionless closed die compaction, the particle displacements differ from the affine values by more than 200% in the initial stages of compaction, with a peak deviation at $D \sim 0.83$. Much less particle rearrangement occurs when inter-particle friction is present: the average displacement deviation from affine motion is less than 50% for $\mu \geq 0.1$, and has a negligible dependence upon the additional constraint of no particle rotation. It is clear from Fig. 7(a) (b) that the degree to which local rearrangement occurs is insensitive to the direction of the macroscopic strain path: the degree of displacement deviation for closed die and hydrostatic compaction is similar.

It is of interest to explore the degree to which the relative tangential displacement of particle centres deviates from that given by affine motion: tangential displacements over and above the affine value indi-

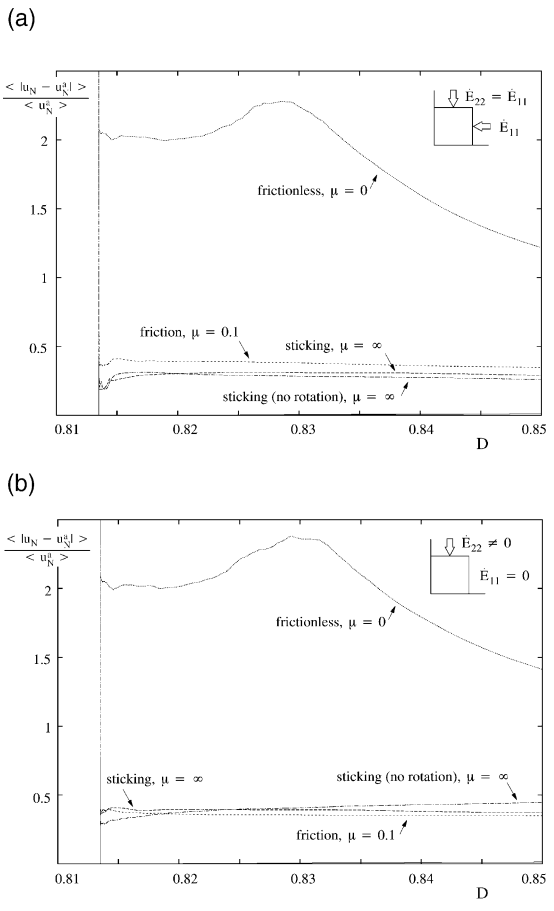

Fig. 7. The average deviation of the actual, realtive normal displacement in the network from the affine relative normal displacement versus density, *D*. Results of various degrees inter-particle friction are shown for (a) hydrostatic compaction and (b) closed die compaction.

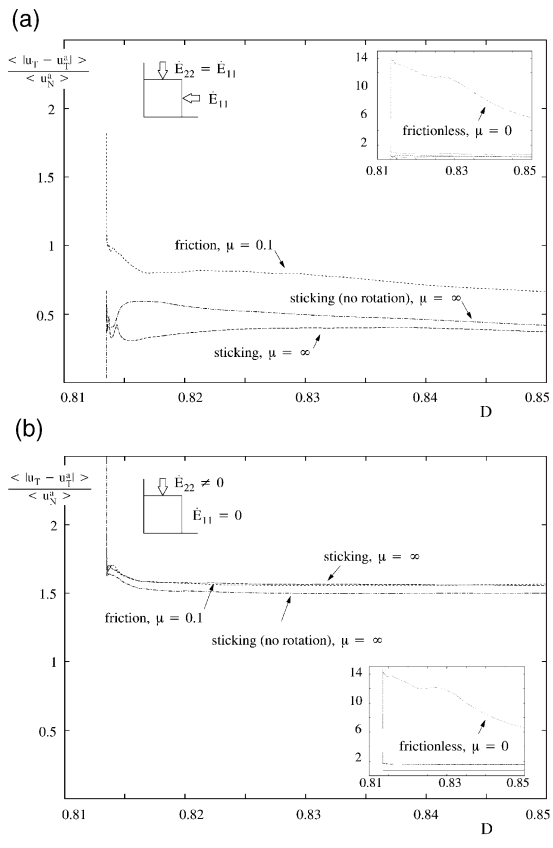

Fig. 8. the average deviation of the actual, relative tangential displacement in the network from affine relative tangential displacement normalised by the affine normal displacement versus density, *D*. Results of various degrees of inter-particle friction in the polydispersed packing are shown for (a) hydrostatic compaction and (b) closed die compaction.

cate local particle rearrangement by a combination of sliding and rolling. A useful measure of the deviation in tangential displacement is given by the ratio $<|u_T - u_T^A|>/<u_N^A>$, where u_T is the relative sliding displacement at each contact [see equation (5)], and u_T^A is the relative tangential displacement of neighbouring particle centres according to affine motion. Consider first hydrostatic compaction. The tangential displacement between two neighbouring particles undergoing affine motion u_T^A equals zero. However, the discrete element calculations give large relative tangential displacements, u_T, as shown in the plot of $<|u_T - u_T^A|>/<u_N^A>$ versus D in Fig. 8(a); the sliding displacements are particularly large for frictionless particles, necessitating the use of a separate scale in the insert of the figure. The degree of particle sliding reduces with an increase in friction level, but remains non-negligible ($<|u_T - u_T^A|>/<u_N^A> \sim 0.5$) in the sticking limit, $\mu = \infty$. Similar curves for closed die compaction are shown in Fig. 8(b). Here, the affine relative tangential displacement is not equal to zero but $<|u_T^A|/u_N^A> \approx 0.80$ throughout the compaction history. The deviation in tangential displacement for frictionless particles is very similar to that for hydrostatic compaction, with an initial peak value of $<|u_T - u_T^A|>/<u_N^A> \sim 14$. When friction is present, the curves plateau rather quickly at about $<|u_T - u_T^A|>/<u_N^A> = 1.5$, compared with a plateau value of about 0.5 for the case of hydrostatic compaction. The deviations in tangential displacement are fairly insensitive to the degree of particle rolling, as illustrated in Fig. 8(a) and (b) for the case $\mu = \infty$; we conclude that particle rolling plays a more minor role than particle sliding in the local rearrangement of particles.

3.4. Yield surface evaluation

In order to calculate the yield surface of a random array of cylinders, the discrete element method is used to compact the polydispersed particle array to a density of $D = 0.85$ along both a hydrostatic and a closed die strain path. The array is then unloaded elastically and subsequently reloaded along the full range of in-plane strain paths in order to probe the yield surface. During reloading, an approximately linear relationship between stress and density exists until yielding occurs. The yield point is defined as the value at which the stress–density curve has a local

maximum in curvature; this corresponds approximately to defining yield at an offset strain of about 0.1%. In order to treat elastic unloading, the unloading and reloading spring stiffness in the normal direction at each contact is set to 10^3 times the loading stiffness. Numerical experimentation shows that the yield points are independent of the exact value of the unloading–reloading stiffness as long as it is sufficiently high.

The yield surfaces for the particulate aggregate with a random dispersion of cylinder radii r in the range $r = R[0.9,1.1]$ are shown in Fig. 9(a) and (b) after hydrostatic compaction and closed die compaction, respectively. The yield surface is plotted by linear interpolation between individual yield points; arrows indicate the direction of straining used to probe the yield points. The part of each yield surface approaching $\Sigma_{11} = \Sigma_{22} = 0$ is hand-sketched.

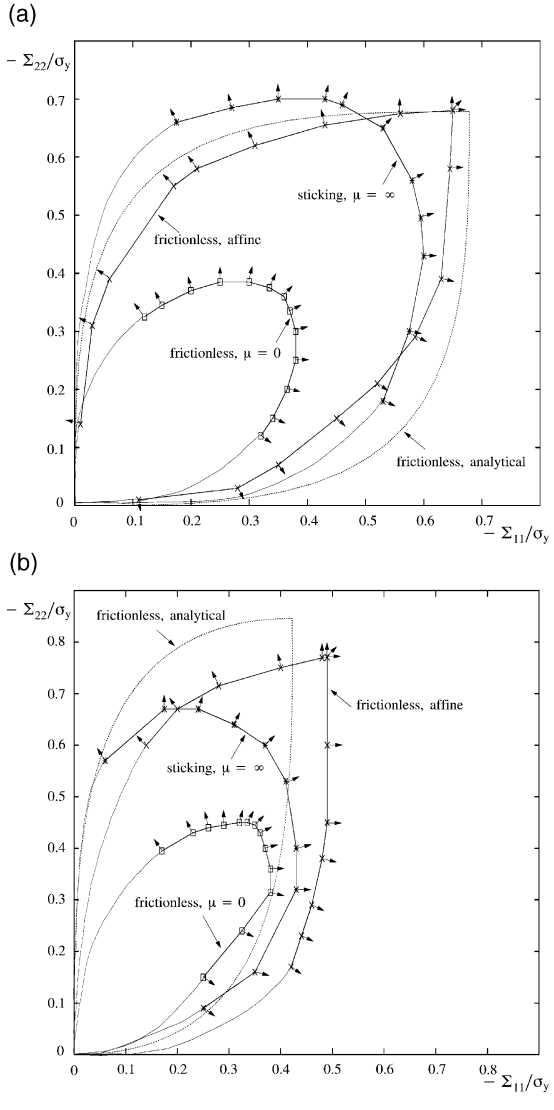

Fig. 9. Yield surfaces of the polydispersed packing, $r = R[0.9,1.1]$, compacted to a density of $D = 0.85$. Various degrees of friction and boundary conditions are shown for (a) hydrostatic precompacts and (b) closed die precompacts. The arrows denote the strain path directions during reloading.

The yield surfaces for hydrostatic compaction are shown in Fig. 9(a) for frictionless and sticking contacts, and for the affine case with frictionless contacts. For comparison, the 2D version of an isotropic yield surface is included, as reported in [3, 19] and as summarised in Appendix A. This upper bound analytical approximation of the yield surface assumes frictionless, cohesionless contacts. When affine boundary conditions are applied to all frictionless particles in the network, a yield surface similar to the analytical yield surface is obtained: the size and shape, with the characteristic vertex at the loading point are each reproduced. The direction of the plastic flow is not uniquely determined at the vertex, as shown by the arrows pointing in different directions. Next, consider the yield surface for the frictionless array of particles; local rearrangement of the particles gives a yield surface which is about half the size of the yield surface due to affine deformation. Furthermore, the yield surface is smooth at the loading point, with the vertex absent. The effect of sticking friction, $\mu = \infty$, is to produce a smooth yield surface which is comparable in size to that due to affine deformation.

The yield surfaces arising from closed die compaction to the density $D = 0.85$ are shown in Fig. 9(b). Again there is adequate agreement between the yield surfaces for affine deformation based upon an infinite isotropic array of particles, and a finite distribution deposited by the ballistic method. In both cases, a vertex develops at the loading point. In the more realistic discrete element simulation, particle rearrangement is taken into account and the yield surface is rounded in the vicinity of the loading point; a direct comparison with the affine result for the frictionless case shows that the yield surface is reduced in size by a factor of about two. Particle rearrangement by sliding is inhibited by friction, and the yield surface for sticking friction is nearly double the size of that for frictionless contacts, in a similar manner to that noted above for hydrostatic compaction.

Riedel *et al*. [7] and Fleck [2] found that the level of inter-particle friction has only a minor effect upon the size and shape of the yield surface when affine deformation is imposed [2, 7]. Figure 9 shows clearly that friction alters the degree of local rearrangement of particles by sliding, and thereby increases the size of the yield surface.

It remains to be determined whether the increase in size of the yield surface by imposing affine deformation is due to the prevention of local particle rearrangement during compaction or during the subsequent probing of the yield surface. To address this, additional calculations were performed for hydrostatic compaction of the polydispersed array to a relative density of $D = 0.85$. Affine deformation and local rearrangement were each imposed during the compaction step and then during the probing of the yield surface, see Fig. 10. For example, the yield surface

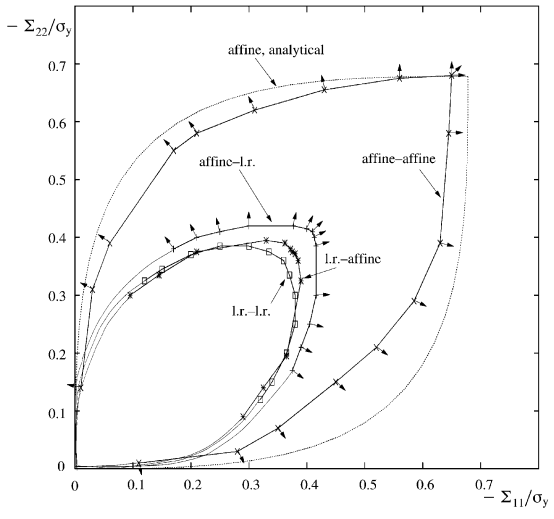

Fig. 10. Yield surfaces of the polydispersed packing, $r = R[0.9,1.1]$, with frictionless inter-particle contacts compacted hydrostatically to a density of $D = 0.85$. Various combinations of boundary conditions during compaction and reloading are shown. The arrows denote the strain path directions during reloading.

labelled "l.r.–affine" refers to compaction by the discrete element method with local rearrangement allowed, followed by probing of the yield surface by imposing affine deformation. The curve labelled "l.r.–l.r." refers to the case where local rearrangement of particles can take place during compaction and during probing of the yield surface, while the curve labelled "affine–affine" denotes the yield surface due to affine motion during both compaction and subsequent probing; both curves are redrawn from Fig. 9(a). We note in passing that each point of the "affine-affine" yield surface was determined unambiguously as the stress–density reloading curves had a sharp knee at the yield point; in contrast, the location of the yield point when local rearrangement was allowed during probing was more ambiguous as the stress–density reloading curves do not possess a sharp knee at yield. Hence, the size of the three yield surfaces involving non-affine motion are accurate to within about 10%; greater confidence can be placed in their shapes, however. It is concluded from Fig. 10 that relaxation of the constraint of affine motion, either during the compaction phase or during the probing of the yield surface, gives rise to the local rearrangement of particles and to a yield surface of about half the size produced by "affine–affine" deformation. Further, local particle rearrangement, either during compaction or during probing of the yield surface leads to a rounding-off of the vertex at the loading point.

4. CONCLUDING REMARKS

In this study the discrete element model has been used to study the compaction of a random distribution of metal circular cylinders, with emphasis placed on the practical cases of hydrostatic and closed die compaction. The significance of inter-particle friction and affine motion has been explored both for the compaction response and for the resulting yield surface.

Consider first the compaction of frictionless particles. Substantial rearrangement takes place in the early stages of compaction and results in low macroscopic stresses both for hydrostatic and closed die compaction. When the friction coefficient is increased, the degree of local particle rearrangement is reduced and a stiffer compaction response is observed. Is has been argued previously [2, 7] that the size and shape of the yield surface exhibit only a minor dependence upon the level of inter-particle friction when the particles move in an affine manner. Figure 9(a) and (b) show that this is not the case when local rearrangement of the particles is accounted for; at the end of Stage I compaction, $D = 0.85$, the yield surface for frictionless particles is about half the size of that for sticking contacts, both for hydrostatic and closed die compaction. The size of the yield surface for sticking contacts is approximately the same as that for affine deformation. Furthermore, the characteristic vertex at the loading point of the yield surface for affine deformation becomes rounded when the particles are free to rearrange in the discrete element model.

The current framework does not guarantee a stable macroscopic response, and under macroscopic strain paths such as those involving a large dilitation it is possible to attain localisation of deformation; then the stiffness matrix of the particle distribution becomes singular. In order to deal with such instabilities, it would be necessary to include the effects of material inertia and damping. However, the scope of the present study is limited to the case of stable compaction involving a large component of hydrostatic compression. For such strain paths, the present approach based on static equilibrium suffices. It is further noted that the effect of plastic indentation at contacts is to redistribute the macroscopic stress uniformly rather than along particular force lines through the particle array. The development of a few loading paths is a characteristic of granular media with elastic-frictional contacts and is not characteristic of a compacting elastic-plastic porous solid.

Acknowledgements—The work of Pia Redanz was financially supported by the FREJA research project, Application of Advanced Material Models in the Analysis of Metal Forming Processes, financed by the Danish Research Agency.

REFERENCES

1. Fleck, N. A., Kuhn, L. T. and McMeeking, R. M., *J. Mech. Phys. Solids*, 1992, **40**(5), 1139.
2. Fleck, N. A., *J. Mech. Phys. Solids*, 1995, **43**, 1409.
3. Storåkers, B., Fleck, N. A. and McMeeking, R. M., *J. Mech. Phys. Solids*, 1999, **47**(4), 785.
4. Kwon, Y. S., Lee, H. T. and Kim, K. T., *Trans. ASME Series H J. Engng Mater. Technol.*, 1997, **119**(4), 366–373.

5. Redanz, P., *Eur. J. Mech. A*, 1999, **18**, 399–413.
6. Redanz, P., *Int. J. Solids Struct.*, 2001, **38**, 759–775.
7. Riedel, H., Meyer, D., Svoboda, J. and Zipse, H., *Int. J. Refract. Met. Hard Mater*. 1993–1994, **12**, 55.
8. Arzt, E., *Acta metall.*, 1982, **30**, 1883.
9. Arzt, E., Ashby, M. F. and Easterling, K. E., *Metall. Trans. A*, 1983, **14**, 211.
10. Helle, A. A., Easterling, K. E. and Ashby, M. F., *Acta metall.*, 1985, **33**(12), 2163.
11. Parhami, F. and McMeeking, R. M., *Mech. Mater.*, 1998, **27**, 111.
12. Newell, K. J., Discrete element modelling of powder consolidation and the formation of titanium matrix comosites from powder-fiber monotapes. Ph.D. thesis, University of California Santa Barbara, 1995.
13. Deutschmann, G., Landis, C. M. and McMeeking, R. M., A network model for the plastic compaction of monodispersed spherical powder, University of California Santa Barbara, 1998.
14. Heyliger, P. R. and McMeeking, R. M., *J. Mech. Phys. Solids*, 2001, **49**(9), 2031.
15. Aparicio, N. D. and Cocks, A. C. F., *Acta metall.*, 1995, **43**(10), 3873.
16. Visscher, W. M. and Bolsterli, M., *Nature*, 1972, **239**, 504.
17. Family, F. and Vicsek, T., *Phys. A: Math. Gen.*, 1985, **18**, L75.
18. Christoffersen, J., Mehrabadi, M. M. and Nemat-Nasser, S., *J. Appl. Mech.*, 1981, **48**(2), 339.
19. Sridhar, I., Fleck, N. A. and Akisanya, A. R., *Int. J. Mech. Sci.*, 2001, **43**(3), 715.
20. Gurson, A. L., *Technol.*, 1977, **99**, 2.

APPENDIX A

A.1. Derivation of 2D analytical yield surfaces

Upper bound estimates of the macroscopic yield surface for a random aggregate of equi-sized, rigid-perfectly plastic spheres are derived in [1, 2] by assuming the affine motion of particles, with isolated plastic dissipation at contacts. For comparison purposes, 2D versions of these yield surfaces have been derived for cohesionless and frictionless powder material using the same procedure as outlined in [1, 2, 3, 19].

A uniform macroscopic strain, $E_{\alpha\beta}$ ($\alpha,\beta = 1$ and 2), is imposed on the powder aggregate and the relative normal displacement of two particles follows from equation (16) as

$$\dot{u}_N = -2Rn_\alpha n_\beta \dot{E}_{\alpha\beta} = -2R(\dot{E}_{11}\cos^2\phi + \dot{E}_{22}\sin^2\phi) \tag{A1}$$

where R is the particle radius, n_α is the unit vector along the line of particle centre, and ϕ is the angle between the 1-direction and the contact normal. The total dissipation rate per contact is

$$\dot{W}_c = 3\sigma_y A_c \frac{\dot{u}_N}{2} \tag{A2}$$

where $3\sigma_y A_c$ is the normal force at the contact and the factor of 1/2 arises because the plastic dissipation is shared between the two particles at each contact. The average plastic dissipation rate over the surface S of each particle is

$$\dot{W}_p = \int_S \left[\frac{Z_0 \dot{W}_c}{2\pi R_0}\right] dS \tag{A3}$$

where Z_0 equals the average number of contacts per particle (assumed constant). The expression for $\dot{W}_p$ must be multiplied by D/V_p, where V_p is the volume of the particle, in order to compute the plastic dissipation per unit macroscopic volume

$$\dot{\bar{W}} = \int_S \left[\frac{Z_0 \dot{W}_c}{2\pi R_0}\frac{D}{\pi R_0^2}\right] dS = \frac{-12\sigma_y D Z_0}{\pi^2}\int_0^{\pi/2} [\sqrt{-2(\dot{E}_{11}\cos^2\phi + \dot{E}_{22}\sin^2\phi)}(\dot{E}_{11}\cos^2\phi + \dot{E}_{22}\sin^2\phi)]d\phi \tag{A4}$$

Following Gurson [20], the macroscopic stress on the yield surface corresponding to any macroscopic strain rate $\dot{E}_{\alpha\beta}$ is obtained by differentiation of $\dot{\bar{W}}$ with respect to $\dot{E}_{\alpha\beta}$, viz

$$\Sigma_{\alpha\beta} = \frac{\partial \dot{\bar{W}}}{\partial \dot{E}_{\alpha\beta}} \tag{A5}$$

The yield surface due to hydrostatic compaction, Fig. 9(a), has been derived in [19].

A.2. Yield surface due to closed die compaction

Closed die compaction comprises the strain path $E_{22}<0$ and all other $E_{\alpha\beta} = 0$. The plastic dissipation per unit macroscopic volume equation (4) is then expressed by

$$\dot{\bar{W}} = -\frac{12\sigma_y D Z_0}{\pi^2}\sqrt{-2E_{22}}\int_0^{\pi/2} \sin\phi(\dot{E}_{11}\cos^2\phi + \dot{E}_{22}\sin^2\phi)d\phi \tag{A6}$$

The macroscopic yield surface for $\dot{E}_{11}<0$ and $\dot{E}_{22}<0$ follows as

$$\Sigma_{11} = -\frac{4}{\pi^2} D Z_0 \sigma_y \sqrt{-2E_{22}} \tag{A7}$$

$$\Sigma_{22} = -\frac{8}{\pi^2} D Z_0 \sigma_y \sqrt{-2E_{22}} \tag{A8}$$

With the loading angle defined by $\theta_c = \text{atan}(\sqrt{\dot{E}_{11}\dot{E}_{22}})$, the yield surface for $\dot{E}_{11}>0$ and $\dot{E}_{22}<0$ is

$$\Sigma_{11} = -\frac{4}{\pi^2} D Z_0 \sigma_y \sqrt{-2E_{22}} \cos^3\theta_c \tag{A9}$$

$$\Sigma_{22} = -\frac{12}{\pi^2} D Z_0 \sigma_y \sqrt{-2E_{22}} \left(\cos\theta_c - \frac{1}{3}\cos^3\theta_c\right) \tag{A10}$$

and for $\dot{E}_{11}<0$ and $\dot{E}_{22}>0$ is

$$\Sigma_{11} = -\frac{4}{\pi^2} D Z_0 \sigma_y \sqrt{-2E_{22}} \left(1 - \cos^3\theta_c\right) \tag{A11}$$

$$\Sigma_{22} = -\frac{12}{\pi^2} D Z_0 \sigma_y \sqrt{-2E_{22}} \left(\frac{2}{3} - \cos\theta_c + \frac{1}{3}\cos^3\theta_c\right) \tag{A12}$$

The above analytical description of the yield surface is plotted in Fig. 9(b).